



CHORUS

This is the accepted manuscript made available via CHORUS. The article has been published as:

Spin-Wave-Mode Coexistence on the Nanoscale: A Consequence of the Oersted-Field-Induced Asymmetric Energy Landscape

Randy K. Dumas, E. Iacocca, S. Bonetti, S. R. Sani, S. M. Mohseni, A. Eklund, J. Persson, O. Heinonen, and Johan Åkerman

Phys. Rev. Lett. **110**, 257202 — Published 18 June 2013

DOI: [10.1103/PhysRevLett.110.257202](https://doi.org/10.1103/PhysRevLett.110.257202)

Spin wave mode coexistence on the nano-scale: A consequence of the Oersted field induced asymmetric energy landscape

Randy K. Dumas^{1,†,*}, E. Iacocca^{1,†}, S. Bonetti², S.R. Sani^{3,4}, S.M. Mohseni^{3,4}, A. Eklund⁵, J. Persson⁴, O. Heinonen^{6,7}, and Johan Åkerman^{1,3,4}

¹Physics Department, University of Gothenburg, 412 96 Gothenburg, Sweden

²Stanford Institute for Energy and Materials Science, Stanford University, Stanford, CA, USA

³Materials Physics, School of ICT, Royal Institute of Technology (KTH), 164 40 Kista, Sweden

⁴NanOsc AB, 164 40 Kista, Sweden

⁵Devices and Circuits, School of ICT, Royal Institute of Technology (KTH), 164 40 Kista, Sweden

⁶Materials Science Division, Argonne National Laboratory, Lemont, IL 60439 USA

⁷Department of Physics and Astronomy, Northwestern University, Evanston IL 60208, USA

It has been argued that if multiple spin wave modes are competing for the same centrally located energy source, as in a nanocontact spin torque oscillator, that only one mode should survive in the steady state. Here, the experimental conditions necessary for mode *coexistence* are explored. Mode coexistence is facilitated by the local field asymmetries induced by the spatially inhomogeneous Oersted field, which leads to a physical separation of the modes, and is further promoted by spin wave localization at reduced applied field angles. Finally, both simulation and experiment reveal a low frequency signal consistent with the intermodulation of two coexistent modes.

PACS numbers: 75.30.Ds, 85.75.-d, 75.78.Cd

*Corresponding Author: randydumas@gmail.com

†These authors contributed equally to this work.

Interest in spin wave (SW) based electronics, also known as magnonics [1, 2], has resulted in increased research geared towards the reliable generation, manipulation, and detection of SWs. Spin transfer torque [3-5] offers an efficient means to convert a dc current into GHz magnetization oscillations, and is therefore ideally suited as a local and intrinsically nanoscale SW injector [6-8]. Nanocontact based spin torque oscillators (NC-STOs) [9-11] offer an ideal platform to study SW generation, owing to their extended free layer which allows for unencumbered SW propagation. A popular school of thought regarding multi-mode generation centers on the fact that if each mode is competing for the same centrally located energy source, provided by the spin transfer torque of a single NC, only one mode should survive in the steady state [12]. This “survival of the fittest” approach is in analogy to two species competing for the same food supply. Furthermore, the highly non-linear nature of STOs will only tend to promote the exponential increase of a single mode. However, as evidenced in both experiments [13-19] and simulations [13, 15] clear signatures of mode-hopping are often observed. In this case, while the system is free to explore two or more modes; at any given instant the system can only be found in a single mode. In this Letter, we present a third possibility, namely that under the correct experimental conditions true mode *coexistence* can be realized in NC-STOs. Mode coexistence is facilitated by the local field asymmetries induced by the spatially inhomogeneous Oersted field in the vicinity of the NC and further promoted by mode localization at reduced field angles.

The seminal work of Slonczewski [20] predicted exchange dominated propagating SWs when the free layer is magnetized perpendicularly. The subsequent experimental work of Bonetti *et al.* [15] and Madami *et al.* [6] then clearly demonstrated the Slonczewski-like propagating mode. Interestingly, the experimentally observed dynamical processes were shown

to vary dramatically when the free layer is magnetized in-plane [10]. Furthermore, the behavior becomes significantly more complex as the free layer magnetization is biased at intermediate oblique angles. To summarize, while the linear propagating Slonczewski mode is stable for all applied field angles, only below a certain critical applied field angle, $\theta < \theta_C$, does a second fundamentally different type of SW excitation also become energetically favorable. This second mode is classified a highly non-linear localized SW bullet, as found both analytically [21, 22] and in micromagnetic simulations [23]. Simulations [15] and experiments [14] then provided evidence of mode-hopping between the propagating and localized modes for $\theta < \theta_C$.

Samples for this study are based on NC-STOs. A circular NC of diameter d is defined through a SiO₂ insulating layer using e -beam lithography on top of a 16 $\mu\text{m} \times 8 \mu\text{m}$ spin valve mesa. The magnetically active portion of the mesa is composed of a (nominal thicknesses in nm) Co(8)/Cu(8)/Ni₈₀Fe₂₀(4.5) pseudo spin valve stack deposited by magnetron sputtering. The Ni₈₀Fe₂₀ and Co play the role of the *free* and *fixed* layers, respectively. All measurements were performed at room temperatures utilizing in a highly uniform and precisely rotatable field with a fixed magnitude of $\mu_0 H = 0.965$ T produced by a Halbach array of permanent magnets; further details can be found in Ref. [24]. Finally, microwave excitations were only observed for a negative current polarity corresponding to electron flow from the free to the fixed magnetic layer.

Micromagnetic simulations were carried out using the MuMax2 code [25]. The simulation volume comprises only the Ni₈₀Fe₂₀ layer and is a disk with a diameter of 1000 nm with a cell size of 3.9 \times 3.9 \times 4.5 nm³ and highly absorbing ($\alpha=1$) boundaries to minimize SW reflections. A uniform spin-polarized current then acts on a sub-volume of the free layer with diameter d , matching the nominal experimental NC diameter. The current-induced Oersted field

is also included in the simulations assuming current flow along an infinite cylinder [26]. The material parameters used for the $\text{Ni}_{80}\text{Fe}_{20}$ are a saturation magnetization $\mu_0 M_S = 0.88$ T, as determined by ferromagnetic resonance (FMR) measurements, exchange constant $A = 1 \times 10^{-11}$ J/m, anisotropy $K = 0$ J/m³, and dimensionless damping parameter $\alpha = 0.01$. The internal magnetization angle, which sets the spin polarization angle, of the Co fixed layer ($\mu_0 M_S = 1.7$ T) is evaluated by solving the magnetostatic boundary conditions in an external field of $\mu_0 H = 0.965$ T applied at an angle θ with respect to the film plane. A spin torque efficiency of 0.3 is used and provides excellent quantitative agreement with the experimentally observed frequencies. Finally, no interlayer exchange coupling between the fixed and free layers is taken into account and the simulations were performed at $T = 300$ K following Brown's thermal field formulation [27]. Micromagnetic simulations that take into account the dynamics in both the fixed and free layers are in agreement with those presented here [28].

The angular dependence of the generated microwave signals at a constant current of $I_{dc} = 20$ mA for a device with a nominal NC diameter of $d = 90$ nm is shown in Fig. 1(a) and are consistent with a prior report [15]. Above the critical angle, $\theta_C \approx 60^\circ$, only a single mode with an oscillation frequency above the FMR frequency of the $\text{Ni}_{80}\text{Fe}_{20}$ film is observed and has been attributed to a propagating SW [6, 15] in the $\text{Ni}_{80}\text{Fe}_{20}$ layer. However, for applied field angles less than θ_C a second mode with a frequency far below the FMR frequency, corresponding to the localized SW bullet, also exists [15, 21]. The angular dependence of the peak power and linewidth are shown in Fig. 1(b) and 1(c), respectively. The dramatic drop in power of the propagating mode for $\theta < \theta_C$ is expected given the available energy now has to be shared, while the increase in linewidth has been attributed to mode-hopping [14]. Observed within the angular range $40^\circ < \theta < \theta_C$ is a broad low frequency ($f < \sim 2$ GHz) signal that can also be attributed to mode-

hopping. As the applied field angle is reduced below 45° the linewidth shows an order of magnitude decrease accompanied by a small increase in peak power for each mode. Most interestingly, this decrease (increase) in linewidth (power) is coincident with the applied field angle at which the frequency of the propagating mode becomes lower than the FMR frequency, suggesting that the localization of the propagating mode improves the quality of each mode. Even though the higher frequency propagating mode drops below the FMR frequency for low angles, and will become highly localized in nature, we will continue to refer to this highest frequency mode as the propagating mode in order to stress that this is the same mode that propagates at higher angles. We should also note that mode localization at reduced field angles has important consequences for potential magnonics applications where the transport of information via propagating SWs is desired. Finally, for $\theta < 20^\circ$ the power of each mode decreases below experimental detection as the precession angle of each mode becomes vanishingly small [14].

Micromagnetic simulations for $I_{dc} = -20$ mA and a NC diameter of $d = 90$ nm, Fig. 1(d), quantitatively reproduce all of the experimentally observed behavior, including the broad low frequency signal for $40^\circ < \theta < \theta_C$. The simulated time evolution of the normalized M_x component averaged under the NC at $\theta = 45^\circ$ is shown in Fig. 1(e). The simulated M_x component randomly switches from being predominately parallel to anti-parallel with respect to the in-plane component of the external bias field, which is directed along the $+x$ direction. Similarly, the smoothed pseudo-Wigner-Ville distribution of the device resistance, Fig. 1(f), exhibits a random evolution of the generated frequencies. Prior simulations revealed that the trajectory of the localized mode lies anti-parallel to the external field direction [14, 29]. This erratic behavior is then consistent with a random mode-hopping between the propagating and localized modes

which predominately oscillate parallel and anti-parallel to the external bias field direction, respectively. Additionally, we can now understand the origin of the broad low frequency signal as arising from the relatively slow and highly stochastic mode-hopping. Also evident in the simulated spectra for $20^\circ < \theta < \sim 45^\circ$ is a weak and narrow low frequency signal that occurs at exactly the difference between the localized and propagating modes, as shown in Fig. 2 for $\theta = 30^\circ$. This is consistent with the 2nd order intermodulation signal of the localized (f_L) and propagating (f_P) modes occurring at $f_P - f_L$. This intermodulation signal is not apparent in the experimentally observed spectra, Fig. 1(a), but may be below our experimental detection limit. Simulations with varying NC diameters, and a constant current density of $J = 5.19 \times 10^{12}$ A/m², reveal that this intermodulation signal not only always occurs exactly at the difference between the localized and propagating mode frequencies, but also becomes significantly more powerful as the NC diameter is decreased, Fig. 2. Simulations for the smallest NC diameter, $d = 60$ nm, also show a 3rd order intermodulation signal at $2f_L - f_P$. Additionally, simulations reveal that the higher order intermodulation peaks also become more pronounced as the applied field magnitude is increased [28]. The 2nd order intermodulation difference signal is routinely measured for a smaller NC diameter of $d = 70$ nm, Fig. 3(a). Fig. 3(a) shows the spectra measured as a function of I_{dc} at a fixed applied field angle of $\theta = 30^\circ$ where both modes are excited. Consistent with a prior report [15] the lower (higher) frequency localized (propagating) mode shows a clear decrease (increase) in frequency as the magnitude of I_{dc} is increased. Correspondingly, the 2nd order intermodulation signal shows a increase in frequency. Micromagnetic simulations, Fig. 3(b), again quantitatively reproduce all of the experimentally observed features including the threshold current, intermodulation signal, and the current tunability (df/dI_{dc}) of each mode. In stark contrast to the behavior observed in Fig. 1(e), the simulated time evolution of the

normalized M_x component, Fig. 3(c), shows a much more regular behavior at an applied field angle of $\theta=30^\circ$. Furthermore, unlike the behavior exhibited at $\theta=45^\circ$, Fig. 1(e), the oscillation trajectory is now primarily opposing the external bias field direction. The characteristic beating pattern shown in Fig. 3(c) is consistent with the simple summation of two coexistent frequencies, as further supported by the smoothed pseudo-Wigner-Ville distribution, shown in Fig. 3(d). Cross-terms, circled in Fig. 3(d), are artifacts arising from the Wigner-Ville transform which actually provide additional information about the relative phase between the two frequencies. The observed behavior reveals that the relative phase relation between the two modes is changing in a well-defined and periodic manner as expected for two coexistent modes.

The spatial distribution of the modes provides additional insights into coexistence and role played by the Oersted field [30, 31]. By separately evaluating the fast Fourier transforms of each simulation cell and filtering each image around the localized, f_L , or propagating, f_P , mode frequencies the spatial profiles of each mode are mapped. The spatial distribution of the propagating and localized modes for $I_{dc}=-18$ mA and $\theta=30^\circ$ are shown in Fig. 4(a) and 4(b), respectively, highlighting that the modes are spatially separated [32]. The localized mode power is primarily confined to an arc around the upper half of the NC diameter, whereas the propagating mode power is centered at a point where the in-plane component of the external field, $H_{//}$, and Oersted field, also shown in Fig. 4(c), produces a local field maximum at the bottom of the NC. At the edge of the NC the strength of the Oersted field is 0.1 T, or $\sim 10\%$ of the external field strength. Such asymmetric mode profiles are reminiscent of what was directly observed using Brillouin light scattering [33]. At $\theta=30^\circ$ each mode lies significantly below the FMR frequency and therefore the energy density of each mode is highly localized. This is in contrast to a higher angles where the frequency of the propagating mode lies well above the FMR

frequency [28]. It is also interesting that the majority of the power for each mode exists in a region just outside the NC diameter. This can be understood by considering the fact that for the region inside the NC the average x -component of the magnetization primarily points to the left, i.e. anti-parallel to $H_{//}$ and schematically represented in Fig. 4(a). However, for the entirety of the region outside of the NC the x -component of the magnetization aligns parallel to $H_{//}$. In order to connect these two regions with opposing magnetization directions the largest angle precessions, and therefore maximum mode power, must occur just outside the boundary of the NC. Finally, the spatial distribution of the low frequency intermodulation mode is shown in Fig. 4(d). This mode is localized below the NC and exhibits a standing wave type pattern due to the physical confinement.

Experimental evidence for the physical separation of the modes can be found in the observed current tunability ($df/d|I_{dc}|$), Fig. 3(a) and 3(b). Prior analytical calculations [21], that do not take into account the Oersted field, predicted that current tunability of the localized and propagating modes would both “redshift”, that is $df/d|I_{dc}| < 0$, for applied field angles less than θ_C . Additionally, micromagnetic simulations confirmed this behavior [23]. However, experiments invariably have found that the high frequency propagating mode “blueshifts” ($df_p/d|I_{dc}| > 0$) for all applied field angles. The changing local magnetic field environment, that is $dH/d|I_{dc}|$, plays a significant role in determining $df_p/d|I_{dc}|$ of the propagating mode. A simple calculation assuming the Oersted field of an infinite wire with a diameter of 70 nm results in $dH/d|I_{dc}| = +56$ Oe/mA on the lower boundary of the NC, where the propagating mode is centered. At a constant I_{dc} the frequency tunability with externally applied field has been measured as $df_p/dH = 2.7$ MHz/Oe. Therefore, based solely on the local field environment at the lower edge of the NC we would expect a current tunability of $df_p/d|I_{dc}| = +0.15$ GHz/mA for the propagating mode, which is

nearly double the observed tunability of $df_p/d|I_{dc}|=+0.07$ GHz/mA. Therefore, the local field environment at the bottom edge of the NC is responsible for flipping the sign of the propagating mode tunability from negative to positive. The physical separation of the modes can also explain the general behavior highlighted in Fig. 2, where it was found that the strength of the intermodulation signal increased as the diameter of the NC decreased. As the NC diameter is decreased, there is more potential for non-linear mixing between the two modes. This results in a more prominent intermodulation signal for smaller NC diameters, consistent with what is also observed experimentally.

In conclusion, evidence of SW mode coexistence on the nanoscale was presented in NC-STOs. While the highly non-linear nature of the STO should promote the existence of only a single mode, the energy landscape is strongly modified by the current induced Oersted field, resulting in multimode coexistence. The spatially inhomogeneous Oersted field in the vicinity of the NC plays two important roles. Firstly, the broken symmetry of the local fields promotes a physical separation of each mode. Experimental evidence of the mode separation lays the observed current tunability of the propagating mode. Secondly, localization of the propagating mode for reduced field angles was found. Together, spatial separation and localization promotes coexistence and results in a distinct intermodulation signal, as also observed experimentally.

Acknowledgements

Support from The Swedish Research Council (VR), The Swedish Foundation for Strategic Research (SSF), and the Knut and Alice Wallenberg Foundation is gratefully acknowledged. Argonne National Laboratory is a US DOE Science Laboratory operated under contract no. DE-AC02-06CH11357 by UChicago Argonne, LLC.

References

1. S. Demokritov and A. N. Slavin, *Magnonics: From Fundamentals to Applications*. (Springer, New York, 2013).
2. V. V. Kruglyak, S. O. Demokritov and D. Grundler, *J. Phys. D: Appl. Phys.* **43**, 264001 (2010).
3. L. Berger, *Phys. Rev. B* **54**, 9353 (1996).
4. D. C. Ralph and M. D. Stiles, *J. Magn. Magn. Mater.* **320**, 1190 (2008).
5. J. C. Slonczewski, *J. Magn. Magn. Mater.* **159**, L1 (1996).
6. M. Madami, S. Bonetti, G. Consolo, S. Tacchi, G. Carlotti, G. Gubbiotti, F. B. Mancoff, M. A. Yar and J. Åkerman, *Nature Nanotechnol.* **6**, 635 (2011).
7. H. Ulrichs, V. E. Demidov, S. O. Demokritov and S. Urazhdin, *Appl. Phys. Lett.* **100**, 162406 (2012).
8. S. Bonetti and J. Åkerman, *Topics in Applied Physics* **125**, 177 (2013).
9. F. B. Mancoff, N. D. Rizzo, B. N. Engel and S. Tehrani, *Appl. Phys. Lett.* **88**, 112507 (2006).
10. W. H. Rippard, M. R. Pufall, S. Kaka, S. E. Russek and T. J. Silva, *Phys. Rev. Lett.* **92**, 027201 (2004).
11. T. J. Silva and W. H. Rippard, *J. Magn. Magn. Mater.* **320**, 1260 (2008).
12. F. M. de Aguiar, A. Azevedo and S. M. Rezende, *Phys. Rev. B* **75**, 132404 (2007).
13. D. V. Berkov and N. L. Gorn, *Phys. Rev. B* **76**, 144414 (2007).
14. S. Bonetti, V. Puliafito, G. Consolo, V. S. Tiberkevich, A. N. Slavin and J. Åkerman, *Phys. Rev. B* **85**, 174427 (2012).

15. S. Bonetti, V. Tiberkevich, G. Consolo, G. Finocchio, P. Muduli, F. Mancoff, A. Slavin and J. Åkerman, *Phys. Rev. Lett.* **105**, 217204 (2010).
16. I. N. Krivorotov, N. C. Emley, R. A. Buhrman and D. C. Ralph, *Phys. Rev. B* **77**, 054440 (2008).
17. K. J. Lee, A. Deac, O. Redon, J. P. Nozieres and B. Dieny, *Nature Mater.* **3**, 877 (2004).
18. P. K. Muduli, O. G. Heinonen and J. Åkerman, *Phys. Rev. Lett.* **108**, 207203 (2012).
19. J. C. Sankey, I. N. Krivorotov, S. I. Kiselev, P. M. Braganca, N. C. Emley, R. A. Buhrman and D. C. Ralph, *Phys. Rev. B* **72**, 224427 (2005).
20. J. C. Slonczewski, *J. Magn. Magn. Mater.* **195**, L261 (1999).
21. G. Gerhart, E. Bankowski, G. A. Melkov, V. S. Tiberkevich and A. N. Slavin, *Phys. Rev. B* **76**, 024437 (2007).
22. A. Slavin and V. Tiberkevich, *Phys. Rev. Lett.* **95**, 237201 (2005).
23. G. Consolo, B. Azzerboni, L. Lopez-Diaz, G. Gerhart, E. Bankowski, V. Tiberkevich and A. N. Slavin, *Phys. Rev. B* **78**, 014420 (2008).
24. S. Bonetti, P. Muduli, F. Mancoff and J. Åkerman, *Appl. Phys. Lett.* **94**, 102507 (2009).
25. A. Vansteenkiste and B. Van de Wiele, *J. Magn. Magn. Mater.* **323**, 2585 (2011).
26. S. Petit-Watelot, R. M. Otxoa and M. Manfrini, *Appl. Phys. Lett.* **100**, 083507 (2012).
27. W. F. Brown, Jr., *Phys. Rev.* **130**, 1677 (1963).
28. See supplemental material for additional information.
29. G. Consolo, G. Finocchio, L. Lopez-Diaz and B. Azzerboni, *IEEE Trans. Magn.* **45**, 5220 (2009).
30. G. Consolo, B. Azzerboni, G. Finocchio, L. Lopez-Diaz and L. Torres, *J. Appl. Phys.* **101**, 09C108 (2007).

31. M. A. Hofer, T. J. Silva and M. D. Stiles, Phys. Rev. B **77**, 144401 (2008).
32. G. Consolo, G. Finocchio, G. Siracusan, S. Bonetti, A. Eklund, J. Åkerman and B. Azzaroni, submitted (2013).
33. V. E. Demidov, S. Urazhdin and S. O. Demokritov, Nature Mater. **9**, 984 (2010).

Figure Captions

FIG. 1 (color online). (a) Experimentally measured frequencies with corresponding (b) peak power and (c) linewidth and the (d) simulated frequencies as a function of the applied field angle for a NC-STO with a nominal NC diameter $d=90$ nm at a measurement current of $I_{dc}=-20$ mA. (e) Time evolution of the M_x/M_S component of the magnetization and (f) smoothed pseudo-Wigner-Ville distribution of the simulated device resistance averaged under the NC for $\theta=50^\circ$. The smoothed pseudo-Wigner-Ville distribution is evaluated using a frequency window of 2 GHz and a time window of 0.1 ns.

FIG 2. (color online). Simulated frequency spectra for several NC diameters at a constant current density of $J=5.19 \times 10^{12}$ A/m² and applied field angle of $\theta=30^\circ$.

FIG. 3 (color online). (a) Experimental and (b) simulated frequencies as a function of I_{dc} for a NC-STO with a nominal NC diameter of $d=70$ nm and applied field angle of $\theta=30^\circ$. (c) Time evolution of the M_x/M_S component of the magnetization and (d) smoothed pseudo-Wigner-Ville distribution of the simulated device resistance averaged under the NC for $I_{dc}=-18$ mA. The

smoothed pseudo-Wigner-Ville distribution is evaluated using a frequency window of 0.4 GHz and a time window of 0.2 ns.

FIG. 4 (color online). Simulated spatial profiles of the (a) propagating, (b) localized, and (d) intermodulation modes for a NC-STO with a NC diameter of $d=70$ nm and applied field angle of $\theta=30^\circ$ and $I_{dc}=-18$ mA. The yellow solid circle defines the NC diameter. The spatial map of the x-component of the Oersted field is shown in (c), where the black solid circle defines the NC diameter.

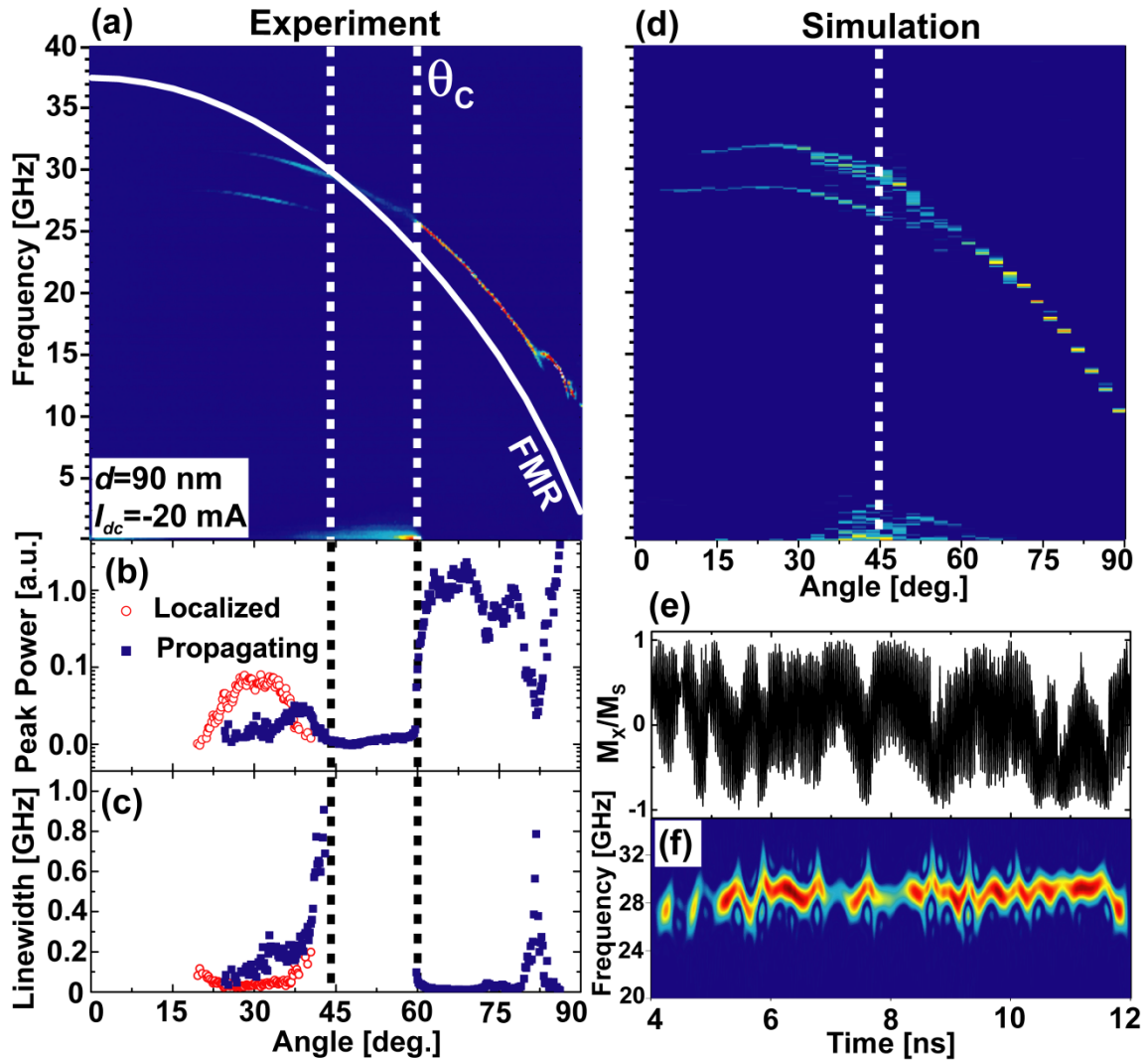


Fig. 1, Dumas *et al.*

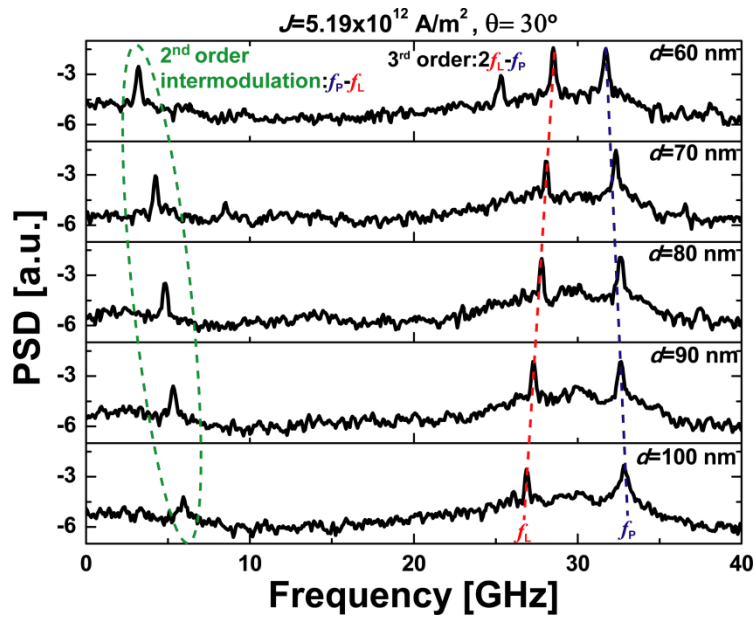


Fig. 2, Dumas *et al.*

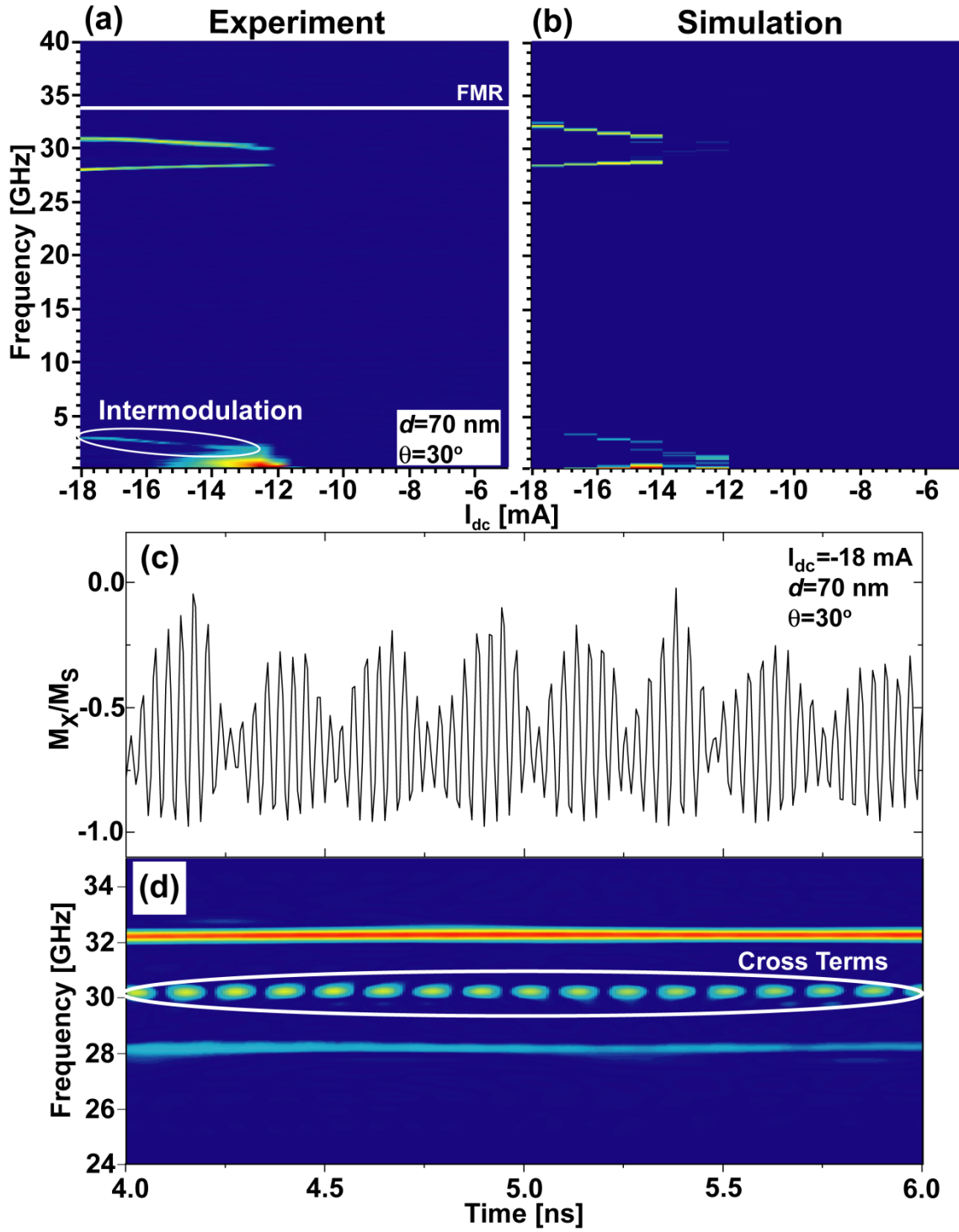


Fig. 3, Dumas *et al.*

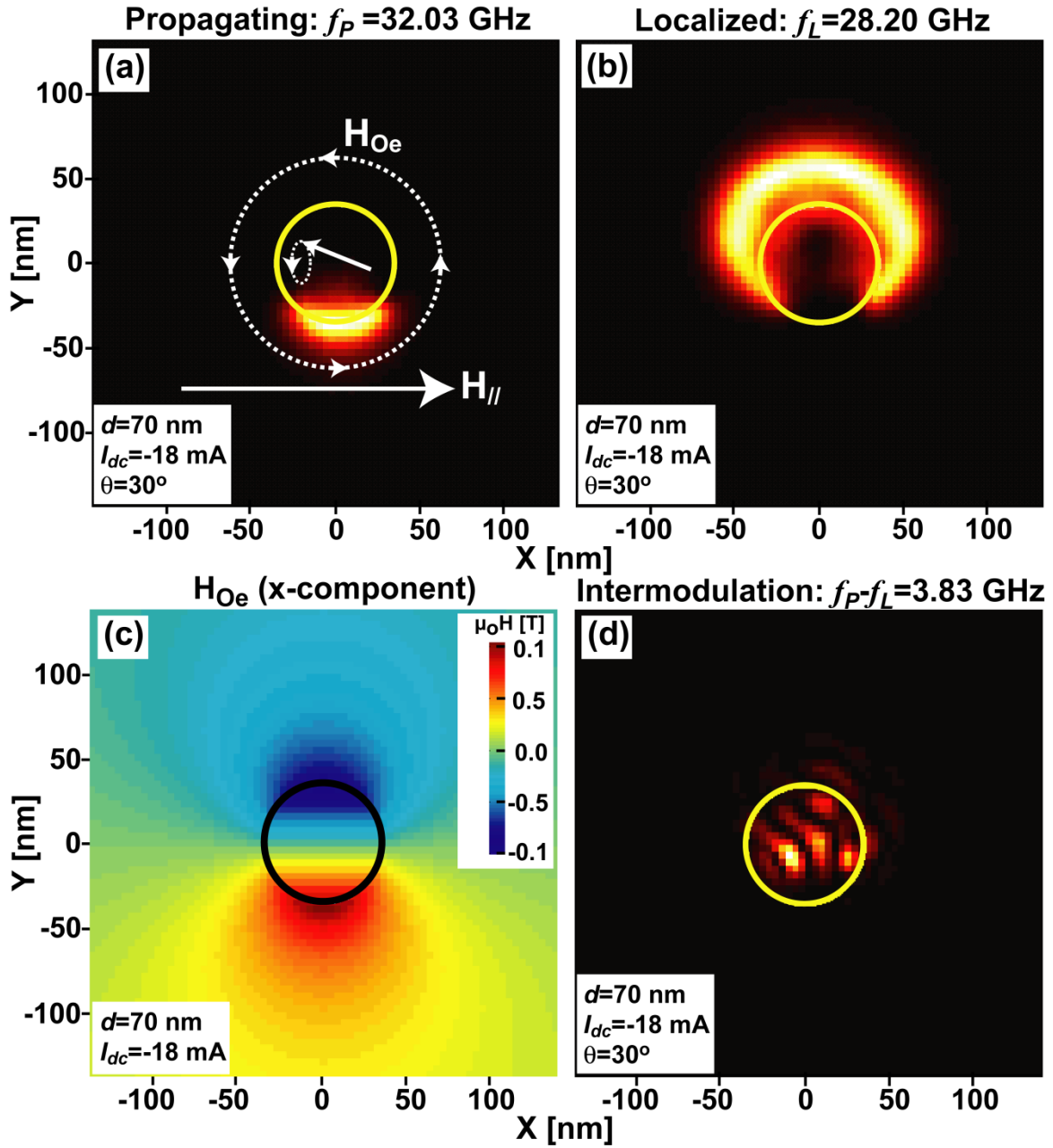


Fig. 4, Dumas *et al.*